Check for updates

PALEONTOLOGY

A ~0.5 Myr perturbation of carbon and mercury cycles during the Middle Triassic biotic radiation

Yiran Cao[1,2], Daoliang Chu[1]*, Runsheng Yin[3], Haijun Song[1], Jacopo Dal Corso[1], Maria Ovtcharova[2], Piero Gianolla[4], Stephen E. Grasby[5], Michael J. Benton[6], Xu Dai[1,7], Greta Alverà[4], Guido Roghi[8], Marcello Caggiati[9], Aya Schneider-Mor[10], Dorit Korngreen[10], Jinnan Tong[1]

Copyright © 2026 the authors; exclusive licensee American Association for the Advancement of Science subject to Canadian Crown copyright, © His Majesty the King in Right of Canada, as represented by the Minister of the Environment, 2026. Distributed under a Creative Commons Attribution NonCommercial License 4.0 (CC BY-NC).

The Anisian Stage (Middle Triassic) marks a pivotal interval for biotic recovery following the Permian-Triassic mass extinction, yet its environmental drivers remain poorly understood. This study presents carbon isotopes, mercury (Hg) concentrations, and Hg isotope data from Anisian (mainly Pelsonian substage) marine and terrestrial sections across the Tethys. Our results reveal a widespread Hg enrichment event that is synchronous with the Pelsonian negative carbon isotope excursion (PENCIE). Hg isotopic compositions support an origin from enhanced regional volcanism, coupled with contemporaneous terrestrial input. New high-precision zircon U-Pb ages (244.200 ± 0.037 Ma and 243.451 ± 0.049 Ma), integrated with chemostratigraphic and biostratigraphic data, constrain the duration of the PENCIE to ~0.5 Myr. This interval coincided with major biodiversification, revealing that recovery occurred alongside environmental perturbations rather than in stable conditions as traditionally thought. These global disturbances in carbon and mercury cycles, linked to volcanism and terrestrial input, likely accelerated Middle Triassic biotic recovery.

INTRODUCTION

In the aftermath of Permian-Triassic mass extinction (PTME), both marine and terrestrial ecosystems were generally biologically depauperate throughout the Early Triassic, experiencing recurrent environmental perturbations that hindered sustained recovery (*1*, *2*). However, recent fossil findings, such as the Guiyang, Paris, Chaohu, and Grippia Bonebed Faunas, demonstrate the existence of complex globally distributed marine ecosystems in the Early Triassic, suggesting an intricate, heterogenous recovery model, variable both in space and time (*3*–*6*). These recovering communities were repeatedly disrupted by ongoing environmental instability (*7*, *8*), preventing full ecological restructuring. A definitive turning point occurred during the Anisian stage, when stable environmental conditions finally facilitated the complete reassembly of ecosystems, marked by the emergence of complex marine communities (e.g., the Qingyan and Luoping/Panxian Faunas) (*9*–*11*) and substantial terrestrial tetrapod radiations (*12*, *13*). From this point onward, ecosystems entered a stage of sustained and stable radiation and development.

The Middle Triassic biotic recovery has been attributed to environmental stabilization, including the restoration of the carbon cycle (C-cycle) (*14*), ocean oxygenation (*15*–*17*), global cooling (*18*), and normal nutrient levels (*19*). However, emerging evidence indicates that this interval was still marked by C-cycle instability, including the Pelsonian negative carbon isotope excursion (PENCIE) in South China (*20*), and local shifts between arid and humid climates documented through sedimentological and palynological studies in Northern Italy (*21*, *22*). Although the PENCIE has been proposed as a potential indicator of Anisian volcanic activity and may have contributed to ecosystem reorganization (*20*), its driving mechanisms, precise timing, correlation across basins, and overall ecological consequences are unknown.

Here, we present a multiproxy geochemical and chronological analysis of marine and terrestrial sections from the Tethyan region. Our study integrates C isotope, mercury (Hg) concentrations, and Hg isotope records from five key sections: Yangwo (YW; South China Block, Eastern Tethys), Dont (DT; Dolomites, Western Tethys), the Ramon 1 (RM) borehole (Israel, northern Gondwana margin), and Linyou (LY) and Xuefeng (XF; North China Block, Northern Tethyan margin) (Fig. 1; see Materials and Methods for more information). High-precision chemical abrasion-isotope dilution-thermal ionization mass spectrometry (CA-ID-TIMS) zircon U-Pb geochronology was applied to volcanic ash beds within the terrestrial sections from North China, providing geochronological constraints for regional and global correlation. On the basis of this integrated dataset, we demonstrate the global nature of the PENCIE, elucidate the origin of associated Hg anomalies, and evaluate its potential ecological impacts.

RESULTS AND DISCUSSION

Zircon U-Pb geochronology and biostratigraphy

The LY and XF sections in North China represent typical terrestrial successions deposited in fluvial-lacustrine environments within the Ordos Basin during the Middle Triassic. Two ash layers from the Upper Member of the Ermaying Formation in the LY and XF sections (Fig. 2, D and E, and figs. S1 and S2) were dated using the CA-ID-TIMS method. The lower ash bed (CSS-4) at the base of the Upper Member of the Ermaying Formation in the LY section yielded a weighted mean $^{206}Pb/^{238}U$ data of 244.200 ± 0.037/0.073/0.27 Ma [2σ, mean square weighted deviation (MSWD) = 0.42, $n = 7$; Fig. 2F

[1]State Key Laboratory of Geomicrobiology and Environmental Changes, School of Earth and Planetary Sciences, China University of Geosciences, Wuhan 430074, China. [2]Department of Earth Sciences, University of Geneva, Geneva 1205, Switzerland. [3]State Key Laboratory of Critical Mineral Research and Exploration, Chinese Academy of Sciences, Guiyang 550081, China. [4]Department of Physics and Earth Sciences, University of Ferrara, via Saragat 1, Ferrara 44122, Italy. [5]Geological Survey of Canada, Natural Resources Canada, Calgary, Alberta T2L2A7, Canada. [6]School of Earth Sciences, University of Bristol, Bristol BS8 1RJ, UK. [7]GeoZentrum Nordbayern, Friedrich-Alexander Universität Erlangen-Nürnberg, Erlangen 91054, Germany. [8]Institute of Geosciences and Earth Resources, IG, National Research Council CNR, Via G. Gradenigo 6, Padua 35131, Italy. [9]Department of Geosciences, University of Padova, Via G. Gradenigo 6, Padua 35131, Italy. [10]Geological Survey of Israel, 32 Yeshayahu Lelbowitz St., Jerusalem 9692100, Israel.
*Corresponding author. Email: chudl@cug.edu.cn

Downloaded from https://www.science.org at University Studi Di Ferrara on June 19, 2026

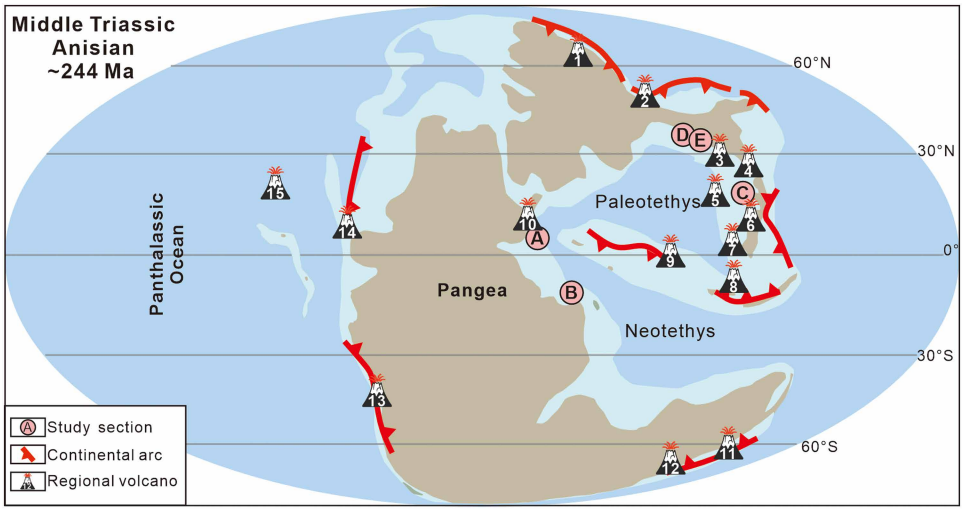


Fig. 1. Paleogeographic reconstruction of the Anisian, Middle Triassic. Paleogeographic reconstruction modified after (*72*). Continental arc data from (*40*). Studied sections: (**A**) DT section (Dolomites); (**B**) RM borehole (Israel); (**C**) YW section (South China); (**D**) LY section (North China); (**E**) XF Section (North China). Locations of contemporary volcanoes: 1. Siberia; 2. Central Asian Orogenic Belt; 3. Kunlun-Tianshan-Tarmi; 4. Qinling; 5. Songpan-Ganzi; 6. South China; 7. Sanjiang; 8: Qiangtang; 9: Lhasa; 10. Southern Alps; 11. New England, Australia; 12. New Zealand; 13. Argentina-Peru; 14. California, USA; and 15. British Columbia, Canada. The source data and references are given in data S6.

and data S1], while the upper ash bed (XF10-5) from the XF section, located approximately 50 m higher than CSS-4, was dated to 243.451 ± 0.049/0.80/0.27 Ma (2σ, MSWD = 1.8, $n = 5$; Fig. 2G and data S1), interpreted as age of zircon crystallization closely approximating the depositional time. These ages correlate with the Pelsonian substage (244.14 to 243.22 Ma) of Anisian Stage as defined in marine sequences (*23*), and are roughly consistent with previous volcanic zircon ages of 244.6 ± 0.51 Ma (MSWD = 0.11, $n = 4$) from the *Balatonites shoshonensis* ammonoid zone in South China (*24*).

The marine sections in this study are constrained by biostratigraphic data, providing age control for the Pelsonian substage (Figs. 2 and 3). In the DT section, ammonoid biostratigraphy reveals a distinct stratigraphic transition: The lower interval belongs to the *Schreyerites binodosus* subzone (late Pelsonian), while the upper interval belongs to *Schreyerites abichi* and *Paraceratites trinodosus* subzones (*25*, *26*). The *Paraceratites* zone containing the *S. abichi* and *P. trinodosus* subzones corresponds to the *Paraceratites trinodosus* zone (*27*), and hence define as the base of the Illyrian in the DT section. Similarly, in the RM borehole, the studied stratigraphic interval (Ra'af and Gevanim formations; Fig. 2B) yields diagnostic ammonoids (*Balatonites balatonicus* and *Schreyerites binodosus* ammonoid zones) that unequivocally indicate a Pelsonian (middle Anisian) age (*28*). This age assignment is corroborated by conodont and foraminiferal evidence from the upper Ra'af Formation (*29*, *30*). In the YW section, conodont biostratigraphy constrains the upper Poduan Formation to the Pelsonian-Illyrian transition (fig. S3) (*20*). The presence of the *Sinokannemeyeria* fauna, a distinct terrestrial vertebrate assemblage with a U-Pb age of ca. 243.53 Ma, in the Upper Member of the Ermaying Formation in Ordos Basin not only provides additional biostratigraphic evidence for the Middle-Late Anisian age (mainly Pelsonian) assignment but also marks the full recovery of terrestrial ecosystems in North China following the PTME (*12*, *31*).

Pelsonian C-cycle perturbation and mercury anomaly

Carbonate and bulk organic C-isotope records ($\delta^{13}C_{carb}$ and $\delta^{13}C_{org}$) from all five sections document coherent trends with regional variations (Fig. 2, A to E). Marine sections show a distinct negative C-isotope excursion (NCIE) during the Pelsonian, with published records from YW and RM revealing characteristic 1 to 2 per mil (‰) shifts in both carbonate and organic carbon phases (*20*, *32*). The RM section displays a large NCIE exceeding 4‰ in the upper Pelsonian, but no distinct phenomenon of positive rebound was observed (Fig. 2B and fig. S4). At DT, we observe $\delta^{13}C_{carb}$ decreasing from +0.2 to −1.1‰ in the lower interval, stabilizing before rebounding to 0.7‰ at the Pelsonian termination. The $\delta^{13}C_{org}$ record shows parallel variation with $\delta^{13}C_{carb}$, declining from −26.4 to −27.5‰ before recovering to between −25.3 and −26.3‰ in the Illyrian, with one anomalous value of −23.1‰. During the early Illyrian, $\delta^{13}C_{carb}$ values are less negative, hovering around 0.1‰ in the DT section (Fig. 2A and fig. S5). The magnitude of the negative $\delta^{13}C_{carb}$ excursion varies considerably among the studied sections (Fig. 2, A to C), with more pronounced and irregular trends observed in relatively proximal or semi-restricted settings, such as YW and RM. These records may have been influenced by local carbon cycling, spatially heterogeneous organic matter remineralization, and early diagenetic overprinting, which can amplify or attenuate primary $\delta^{13}C_{carb}$ signals. In contrast, the more distal, deeper-water DT section yields a stratigraphically coherent $\delta^{13}C_{carb}$ trend, suggesting that it more closely records changes in the global marine $\delta^{13}C_{DIC}$ reservoir.

The terrestrial $\delta^{13}C_{org}$ records from the LY and XF sections correlate with the marine records (Fig. 2). At LY, the Upper Ermaying Formation shows an abrupt 3.2‰ negative shift from −22 to −25.2‰, followed by a transient recovery to −23.1‰ before stabilizing between −25.2 and −24.3‰ (Fig. 2D). Similar dynamics observed in XF section: after averaging −25.5‰ in the Lower Member, $\delta^{13}C_{org}$ values rise to −24.5‰ before declining to −27.4‰ at the base of the Upper Member, then gradually recovering to −24.5‰ before final stabilization around −25.5‰ (Fig. 2F). These consistent marine-terrestrial patterns demonstrate that the PENCIE represents a notable potential global C-cycle perturbation.

The PENCIE is consistently associated with Hg enrichments in both marine and terrestrial depositional environments, although

Downloaded from https://www.science.org at University Studi Di Ferrara on June 19, 2026

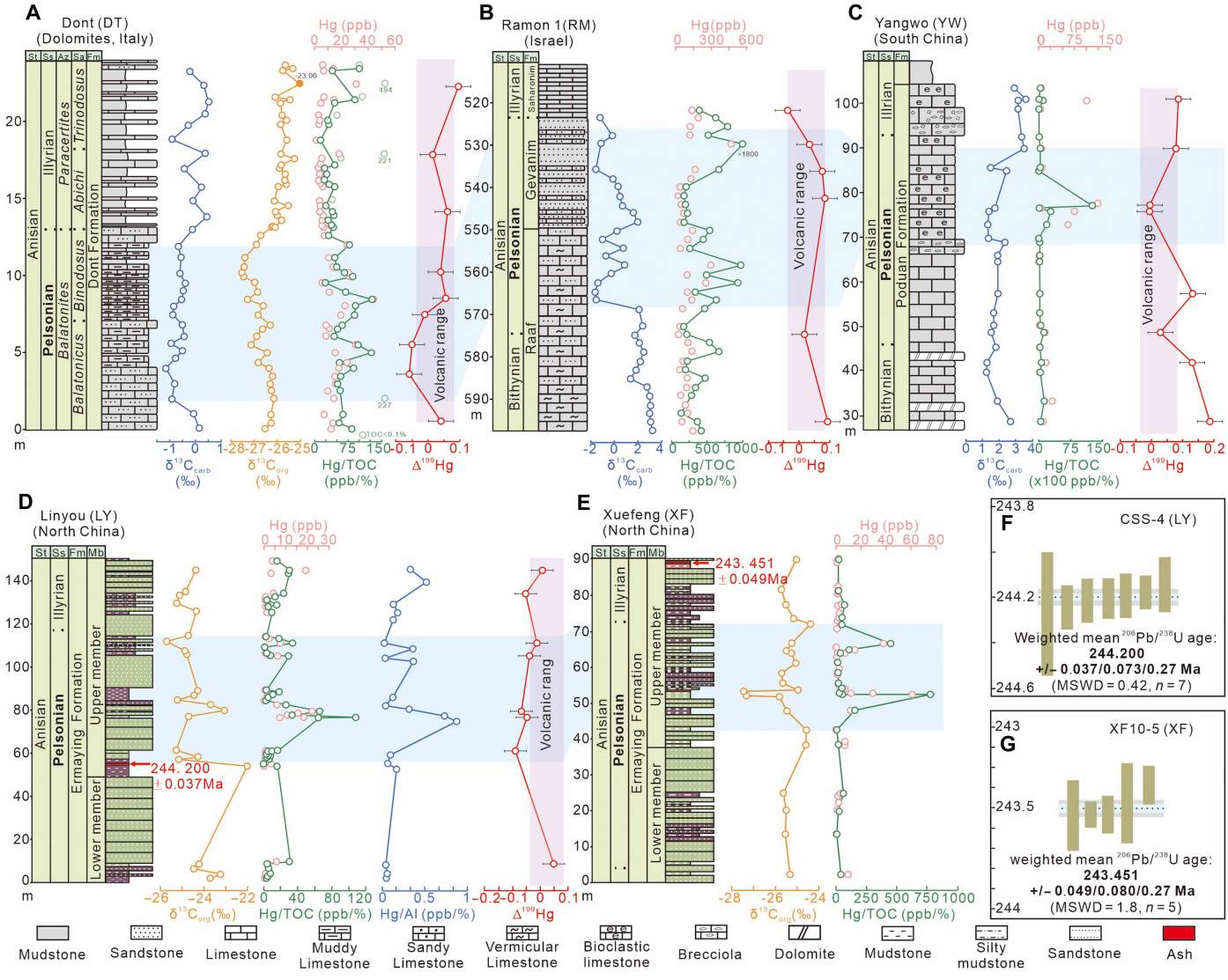


Fig. 2. Profiles of the studied sections. Bulk carbonate and organic C isotope ($\delta^{13}C_{carb}$ and $\delta^{13}C_{org}$), Hg concentrations, Hg/TOC ratios, Hg/Al ratios, and Hg isotope ($\Delta^{199}Hg$) from the Dont (DT) section in the Dolomites, Italy (**A**), Ramon 1 (RM) borehole in Israel (**B**), Yangwo (YW) section in South China (**C**), Linyou (LY) section in North China (**D**), and Xuefeng section (XF) in North China (**E**) and weighted mean and ranked $^{206}Pb/^{238}U$ plot of the analyzed zircon grains from LY (**F**) and XF (**G**). The $\delta^{13}C_{carb}$ and Hg/TOC of YW are from (*20*), and the $\delta^{13}C_{carb}$ and TOC of RM are from (*32*). The blue bar is the interval of PENCIE. St, stage; Ss, substage; Fm, formation: Mb, member; Az, ammonite zone; Sa, ammonite subzone.

the magnitude of these anomalies varies systematically between settings (Fig. 2, A to D). The marine DT section exhibits a well-defined Hg enrichment profile, with concentrations progressively increasing from background levels [~5 parts per billion (ppb)] to a peak of 43.9 ppb at ~8.5 m before returning to baseline values, and this pattern remains evident in Hg/total organic carbon (TOC) ratios (Fig. 2A). The RM borehole shows two more intense Hg anomalies (331 and 503 ppb) that precisely coincide with the NCIE, maintaining elevated Hg/TOC ratios despite weak Hg-TOC covariation (R = 0.1) (Fig. 2B and fig. S6). While terrestrial sections exhibit smaller-amplitude Hg anomalies compared to marine records, they nevertheless preserve clearly identifiable enrichment patterns during the NCIE (Fig. 2, D and E). At LY, Hg concentrations show a distinct threefold increase (6.7 to 19 ppb) compared to background levels (<5 ppb), although the absolute value of the Hg peak is not high (Fig. 2D and fig. S1). The Hg/TOC and Hg/total sulfur (TS) correlation coefficients of LY are 0.52 and 0.17, respectively (fig. S6 and data S2). Similarly, the XF section records two discrete Hg peaks, a prominent 60.9 ppb anomaly aligned with the maximum $\delta^{13}C_{org}$ shift and a secondary 37.7 ppb pulse, with weak correlation between Hg and TOC (R = 0.22), and Hg and TS (R = 0.14). Although these statistical correlations remain insignificant due to low TOC (<0.2% at LY; <0.1% at XF) and TS (≤0.05% at LY; ≤0.01% at XF) contents (fig. S6), the consistent stratigraphic position of Hg/TOC and Hg/TS ratio peaks after the onset of the PENCIE provides robust evidence for synchronous Hg enrichment across marine and terrestrial environments (Fig. 2, A to D). Regional variations in Hg-TOC relationships reveal distinct depositional controls: At DT, Hg

Downloaded from https://www.science.org at University Studi Di Ferrara on June 19, 2026

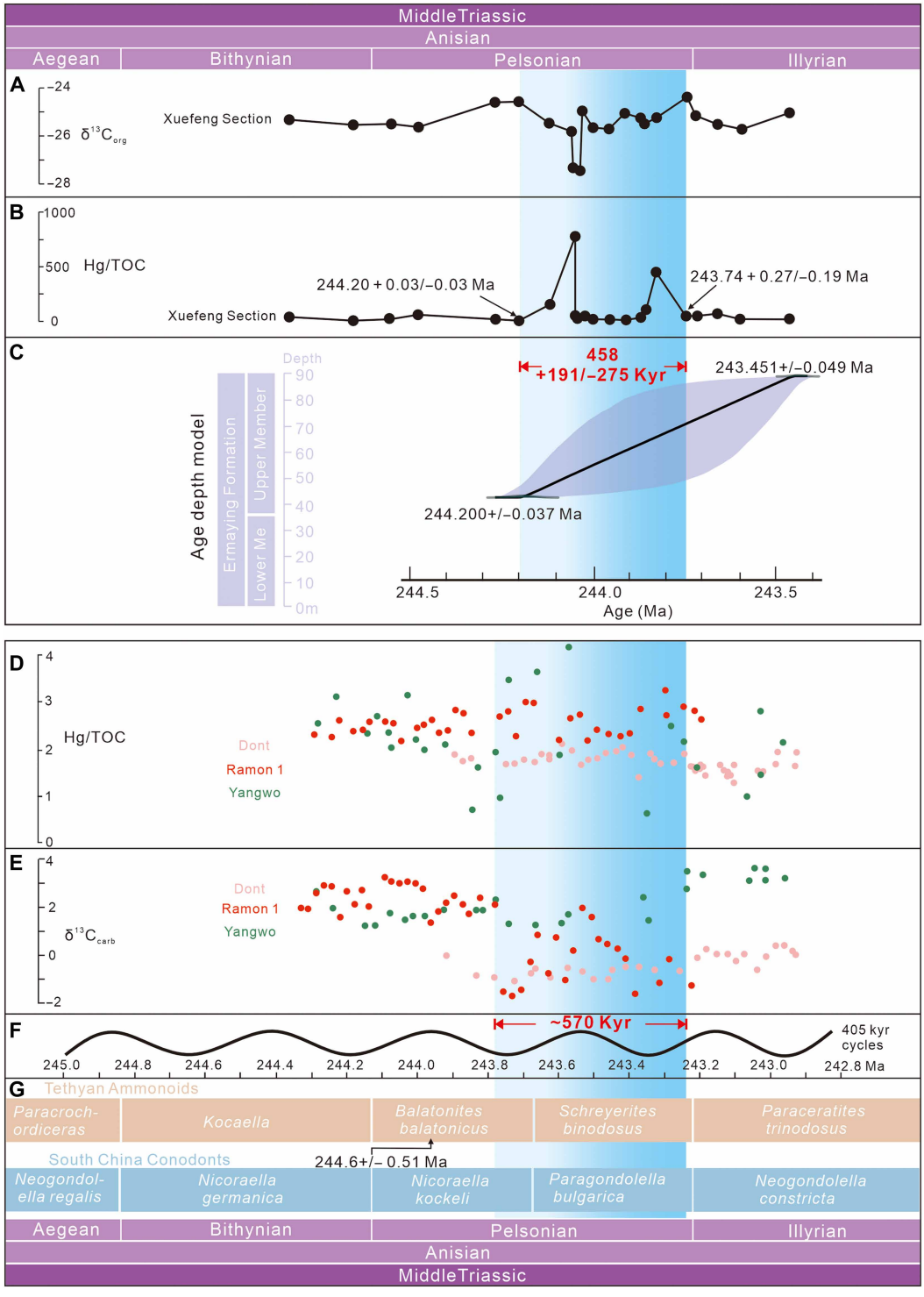


Fig. 3. The duration of PENCIE. (**A**) $\delta^{13}C_{org}$ (‰), (**B**) Hg/TOC (ppb/w%), and (**C**) age-depth model from XF, North China. (**D**) $\delta^{13}C_{carb}$ (‰) and (**E**) Hg/TOC (log_{10} ppb/w%) from DT, RM, and YW sections. (**F**) Astronomically (405 kyr cycle) tuned timescale in the Anisian (*23*). (**G**) Tethyan ammonoid and South China conodont zones in the Anisian (*27*), with U-Pb age from (*24*).

Downloaded from https://www.science.org at University Studi Di Ferrara on June 19, 2026

moderately correlates with TOC ($R = 0.65$ and $P < 0.001$), suggesting organic matter as the primary Hg host. The strong Hg-Al correlation at LY ($R = 0.79$ and $P < 0.001$) indicates that the host of Hg in the North China is mainly composed of terrestrial clay substances (fig. S6). The weak Hg-TOC and Hg-TS correlations at RM and YW, combined with stable sedimentary environments, indicates multiple Hg hosts. In the marine DT and YW sections, Hg and Al show a moderate correlation ($R = 0.51$ and $P < 0.05$) and an essentially absent correlation ($R = 0.01$ and $P > 0.05$), respectively (fig. S6). Although Hg concentrations in our studied sections show varying degrees of enrichment during the PENCIE (Fig. 2), they remain much lower than the Hg accumulation observed during events such as the PTME and Triassic-Jurassic mass extinction (TJME) (fig. S7 and data S3), which were caused by intense eruptions of large igneous provinces (*33*). Volcanic activity during the PENCIE was therefore likely weaker than that associated with large igneous provinces; however, it should be noted that the relationship between Hg (and Hg/TOC) enrichments and volcanic outgassing intensity may be complicated by variations in eruptive style and volcanic gas composition (e.g., Hg and CO_2 ratios) between different types of volcanism (*34*).

Mercury isotopic evidence for volcanic-terrestrial Hg sources during PENCIE

Mass-independent fractionation of Hg isotopes (Δ^{199}Hg) provides critical constraints on mercury provenance (*33*). During the PENCIE interval, all studied sections display coherent negative excursions in Δ^{199}Hg that precisely coincide with Hg enrichment (Fig. 2 and fig. S8). In the LY section, Δ^{199}Hg decreases from +0.05 to −0.09‰ in the mercury-rich interval before recovering to +0.01‰. Similar patterns are observed at YW (decline from >+0.13 to ∼−0.01‰), DT (decline from +0.04 to −0.06‰), and RM (decline from +0.04 to ∼−0.04‰ in the Gevanim Formation's Hg peak), although Hg isotope values were not obtained at the first Hg peak in RM through insufficient sample material (Fig. 2). Odd-mass–independent fractionation of Hg is primarily produced by photochemical processes and resistant to petrological processes, making Δ^{199}Hg capable of tracing the sources of Hg in sedimentary rocks (*35*). In our work, volcanic Hg deposition alone cannot account for the negative Δ^{199}Hg excursions in the studied sections, because Hg derived from volcanic emissions typically displays near-zero Δ^{199}Hg values (*36*). Since terrestrial soils show negative Δ^{199}Hg values, the observed negative excursions require notable contributions from terrestrial erosion (*37*, *38*).

To further evaluate whether the Δ^{199}Hg excursions during the PENCIE could be attributed solely to enhanced terrestrial erosion under intensified hydrologic cycling, we combined the Ternary isotope mixing model of Δ^{199}Hg with independently derived Hg mass accumulation rates (MARs) (approximately the same as Hg flux) constrained by the age-depth model (methods in Supplementary Text). The mixing calculations indicate that both marine and terrestrial sections record non-zero minimum terrestrial fractions (f_t-min > 0) across the PENCIE interval, confirming a measurable terrestrial contribution (fig. S9 and data S4). However, Hg flux values increase markedly during the PENCIE, reaching approximately five to 50 times background levels (fig. S10 and data S5). Assuming that atmospheric Hg deposition remained broadly comparable before and after the PENCIE, a scenario without volcanic input ($f_v = 0$) would require the entire Hg MAR increase to be supplied by enhanced terrestrial erosion ($f_t + f_a = 1$). Under such conditions, the ternary mixing model predicts Δ^{199}Hg values substantially shifted toward the terrestrial endmembers, exceeding the measured values in the LY section. This discrepancy indicates that a purely erosion-driven origin is unlikely to account for both the magnitude of Hg flux enhancement and the observed isotopic composition simultaneously. Instead, the combined isotopic mass balance and flux constraints suggest that the elevated Hg burial rates during the PENCIE were most plausibly driven by the joint effects of volcanogenic and intensified terrestrial delivery Hg contribution.

This interpretation is supported by lithological evidence of enhanced terrigenous input (increased terrigenous debris at DT and $CaCO_3$ depletion at RM) and strong Hg and Al correlation ($R = 0.79$) at LY and moderate correlation at YW ($R = 0.51$), indicating fluvial Hg transport (Fig. 2 and figs. S1 and S5). Although Al concentrations increased in both marine sections during the PENCIE interval (data S2.), the lack of correlation between Hg and Al (fig. S6) in YW, together with its Hg isotopic compositions being closer to the volcanic end-member (Fig. 2C), indicates that the degree of terrigenous influence on Hg accumulation was not uniform across the marine realm. Regional congruence with Sr isotopes (*39*), gamma-ray signatures (*23*), and siliciclastic proxies (*20*) indicate intensified continental weathering during the PENCIE (Fig. 4). On the other hand, relatively high-background subduction-related volcanism was widespread during the Anisian (Fig. 1). Notably, the PENCIE falls within the longest interval of continental arc development since the onset of the Mesozoic, which reached a total length of over 20,300 km (*40*, *41*). Widespread magmatic activity during the Pelsonian along the margins of the Tethys and Panthalassa oceans is documented by isotopic age evidence (Fig. 1 and data S6), as evidenced by studies of the Sanjiang Orogenic Belt (*42*) and the Central Asian Orogenic Belt (*43*). Collectively, these findings demonstrate that Hg entered marine and terrestrial sediments from terrigenous sources through erosion against the background of sustained relatively high arc volcanism.

The duration of PENCIE

Constrained by the two bounding ages (244.200 ± 0.037 Ma and 243.451 ± 0.049 Ma) from the LY and XF sections, the duration of the PENCIE interval can be precisely estimated in North China (Fig. 3, A to C). By integrating chemostratigraphic correlation of synchronous C-isotope and Hg trends (Fig. 2) with an age-depth model (*44*) anchored by two high-precision ages, the upper and lower boundaries of the PENCIE in the XF section can be determined as: 243.74 + 0.21/−0.19 Ma [95% confidence interval (CI)] and 244.20 + 0.03/−0.03 Ma (95% CI), respectively, with a duration of 0.46 + 0.19/−0.27 Myr (95% CI) (Fig. 3C). In addition, the PENCIE is precisely constrained within the Tethyan biostratigraphic framework, enabling its duration to be determined through integrated marine records (Fig. 3, F and G). The excursion spans the *B. balatonicus* to *Schreyerites binodosus* ammonoid subzones in the Southern Alps (*45*) and correlates with the *Nicoraella kockeli* to *Paragondolella bifurcata* conodont zones in South China (*20*, *46*). This correlation is further supported by its occurrence in *Neospathodus* cf. *kockeli*–earing strata in Israel (*32*). Within this biostratigraphic framework, cyclostratigraphic analyses of marine sections indicate that the PENCIE persisted for approximately 0.57 Myr (Fig. 3F) (*23*, *27*). The duration estimates obtained from terrestrial radiometric dating and marine cyclostratigraphy are highly consistent (Fig. 3), constraining

Downloaded from https://www.science.org at University Studi Di Ferrara on June 19, 2026

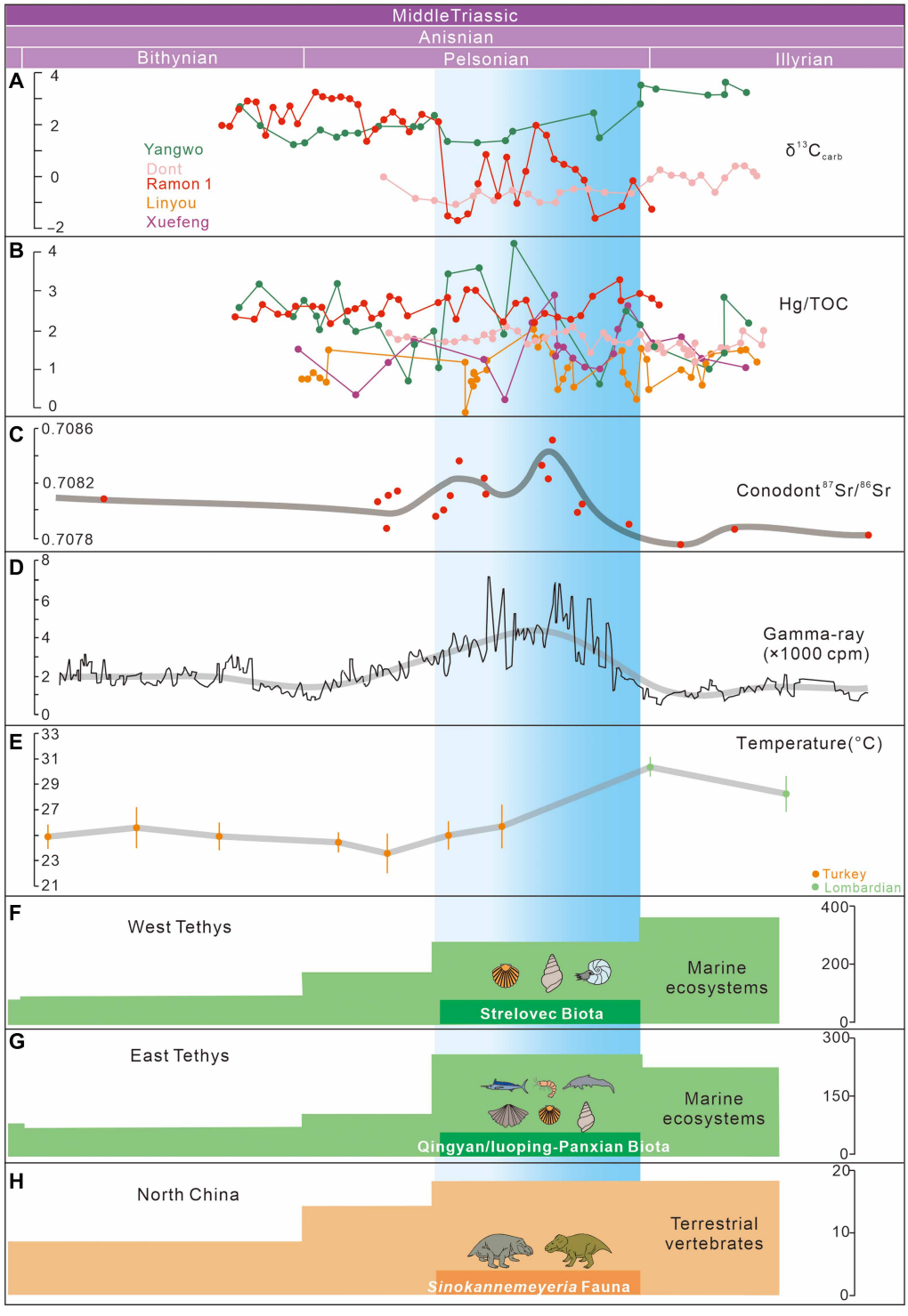


Fig. 4. Environmental changes and biodiversity variations in Anisian, Middle Triassic. (**A**) Marine $\delta^{13}C_{carb}$ (‰) from DT, RM, and YW show negative excursions during the Pelsonian. (**B**) Hg/TOC (log_{10} ppb/w%) from DT, RM, YW, XF, and LY show abnormal enrichments of Hg during PENCIE. (**C**) Conodont $^{87}Sr/^{86}Sr$ (*39*) and (**D**) gamma-ray (*23*) records from South China reveal the enhancement of terrestrial inputs during PENCIE. (**E**) The trend of temperature from conodonts $\delta^{18}O_{phosN}$ shows global warming in the Pelsonian (*18*). (**F**) Number of genera in Western Tethys and (**G**) in Eastern Tethys suggest an explosive biodiversity increase during and after PENCIE. Data on marine ecosystems is from (*2*) and data S7. The representative Streloves biota in western Tethys (*59*) and Luoping-Panxian and Qingyan biotas in Eastern Tethys (*9*–*11*) show the complete restoration of the ecosystem structure. (**H**) Number of terrestrial vertebrate genera in the Anisian (*73*) and *Sinokannemeyeria* fauna (*12*) from North China suggests the rebound of terrestrial ecosystem in the Pelsonian.

Downloaded from https://www.science.org at University Studi Di Ferrara on June 19, 2026

this event to the Pelsonian in both marine and terrestrial environments, and providing evidence for the global nature of PENCIE. The minor discrepancy between the two estimates likely reflects the inherent uncertainties in both orbital tuning (particularly for the Middle Triassic) and radiometric dating, rather than representing true temporal variability in the event itself. On the basis of the integration of marine and terrestrial age data, the duration of the PENCIE and Hg anomalies is estimated to be approximately 0.5 Myr.

The duration and intensity of volcanic activity are key factors that may explain differences in ecosystem responses to environmental perturbations (*47*–*49*). For instance, the PTME was marked by a rapid NCIE of up to −8‰ within 60 kyr (*50*). Similarly, during the TJME, the NCIE reached −5‰ and likely unfolded over less than 290 kyr (perhaps only 70 kyr) (*51*, *52*). In both events, intense and short-lived LIP eruptions triggered major biodiversity losses (*53*, *54*). However, C isotopes show only a perturbation of 1 to 2‰ over ~0.5 Myr during the PENCIE, with a rate of change only 2 to 5% that of the PTME and TJME. The low intensity and slowly release rate of volcanism during the PENCIE may explain why ecosystems did not experience the biotic crisis observed during the PTME and TJME.

Environmental disturbance during the Anisian biological radiation

The PENCIE occurred during a critical phase of marine and terrestrial ecosystem recovery and radiation following the PTME (*20*). Within this biostratigraphical constrained interval, marine biodiversity in both the eastern and western Tethys increased significantly and continuously (Figs. 3 and 4). Nektonic groups such as ammonoids and conodonts, as well as benthic organisms including bivalves and gastropods, all underwent notable proliferation during the late Pelsonian (*55*–*57*). This biodiversification is exemplified by the Qingyan Biota, which is characterized by highly diverse benthic assemblages of gastropods, bivalves, and brachiopods (*9*, *58*), and the Luoping and Panxian biotas, renowned for their rich diversity of marine reptiles, fishes, and arthropods (*10*, *11*), both occurring within the Pelsonian substage. Similar patterns are observed in the Strelovec Biota of the western Tethys, which hosts exceptionally preserved fossils from multiple taxonomic groups (*59*). Terrestrial ecosystems exhibited parallel biological radiation, with vertebrate faunas in North China showing substantial diversification (Fig. 4). The emergence of the *Sinokannemeyeria* fauna, marked by the proliferation of *Kannemeyeria* and pseudosuchians, also dates to the Pelsonian substage (*12*). New high-precision ages from terrestrial successions presented in this study further confirm that the rise of terrestrial tetrapods was comparable to the restoration of marine ecosystems (Fig. 3).

The discovery of carbon cycle disturbances and Hg anomalies during the PENCIE challenges the long-standing view that Middle Triassic ecosystem recovery occurred under prolonged environmental stability (*1*, *2*, *14*). Although the magnitude of these perturbations was lower than during the Early Triassic, coupled carbon and Hg isotope variations indicate a phase of regionally elevated arc volcanism and continental weathering during the Anisian (Fig. 4). Concurrently, a Pelsonian temperature rise in the western Tethys, recorded by conodont apatite oxygen isotopes (Fig. 4) (*18*), would have intensified the hydrological cycle (*22*), and thereby amplified terrestrial nutrient fluxes to marine systems.

In addition, this volcanically driven nutrient pulse may have played a key role in ecosystem restructuring: a moderate increase in terrigenous input against an otherwise stable background could have provided critical short-term nutrient support (*23*, *39*), sustained primarily by volcanic ash deposition and weathering of intermediate to felsic magmas (*48*, *60*). The resulting nutrient enrichment, particularly of phosphorus, stimulated a moderate rise in marine primary productivity that remained within ecologically tolerable thresholds and did not lead to widespread ocean anoxia in upper water column (*16*, *19*). Although elevated primary productivity has been reported from the Luoping Biota during the PENCIE (*46*), evidence for a widespread or global increase in marine nutrient availability during this interval remains limited. This controlled increase in productivity in turn fostered the development of complex trophic structures, as evidenced by multilevel trophic pyramids spanning from benthic organisms to apex predators in biotas such as those of Qingyan, Luoping, and Panxian. Although the PENCIE has primarily been discussed in the context of marine environmental change, intensified hydrologic cycling may also have influenced terrestrial ecosystems by enhancing chemical weathering and nutrient recycling, potentially facilitating gradual ecosystem recovery on land (*61*).

Our study reveals that although the environment was thought to have been relatively stable during the Anisian ecosystem recovery, a critical C and Hg cycle perturbation occurred during the Pelsonian. High-precision geochronology, integrated biostratigraphy, cyclostratigraphy, and Hg-isotope records collectively indicate a transient yet potential globally recognizable NCIE and Hg anomalies, reflecting elevated volcanic activity and enhanced continental input persisting for about ~0.5 Myr. These processes revise the understanding that ecosystem recovery always took place under a stable environmental background. Relatively elevated terrigenous inputs resulting from regional volcanism provided moderate support for ecosystem recovery. The relatively slow rate of environmental change during the PENCIE, evidenced by only a 1 to 2‰ fluctuation in carbon isotopes over more than 0.5 Myr (Figs. 3 and 4), likely played a key role in facilitating recovery.

MATERIALS AND METHODS

Geological setting

The LY section (34°40′45.69″ N, 107°50′18.64″ E) is situated near the Cishansi Temple in LY County, Shaanxi Province. The Middle Triassic here comprises the Ermaying and Tongchuan formations. The section is predominantly characterized by exposures of the Ermaying Formation, with its lower part consisting of thick to extremely thick sandstone beds intercalated with thin layers of purplish-red mudstone. Upward, the succession shows an increase in mudstone content, marked by the appearance of gray-green mudstones. A distinct layer of gray-green clay is developed at the base of the upper member (Fig. 2D and fig. S1).

The XF section (35°33′27.25″ N, 110°14′1.00″ E) is situated along a roadside in Wujiaoshu Village, Huanglong County, Shaanxi Province, adjacent to the XF Reservoir. During the Middle Triassic, this area lay on the southeastern margin of the Ordos Basin. At the XF section, the lower portion is dominated by the Lower Member of the Ermaying Formation, which consists primarily of thick-bedded sandstone. Overlying this is the Upper Member of the Ermaying Formation, characterized by sandstone interbedded with purple-red and green mudstones. A distinct layer of gray-green clay is developed in the upper part of the Upper Member (Fig. 2E and fig. S2).

Downloaded from https://www.science.org at University Studi Di Ferrara on June 19, 2026

The YW section (25°03′37″ N, 105°43′52″ E) is located near YW Village in Ceheng County, Guizhou Province. During the Middle Triassic, this region was situated on the Yangtze Platform, South China, which occupied a position within the eastern Paleo-Tethys Ocean at paleolatitudes of 20-30° N (Fig. 1). The exposed stratigraphic sequence, belonging to the Poduan Formation, has a thickness of approximately 110 m. Conodont biostratigraphy indicates that the upper part of the formation dates to the Pelsonian to Illyrian substages. (Fig. 2C and fig. S3) (*20*).

The DT section (46°21′44.86″ N, 12°08′19.06″ E) is situated on the right bank of the Maè River, near DT Village in the southeastern Dolomites of Italy. This region formed part of the western Tethys during the Middle Triassic (Fig. 1). The exposed succession, assigned to the Dont Formation, is approximately 23 m thick, although its base is covered. The section provides excellent biostratigraphic constraints, primarily through ammonoids, for the Pelsonian to Lower Illyrian interval (Fig. 2A and fig. S5) (*25*, *45*).

The RM borehole (30°35′38.20″ N, 34°52′43.70″ E) was drilled in the Makhtesh Ramon area of the Negev Desert, southern Israel, with a studied depth interval of 522 to 596 m (*32*). The Triassic sedimentary succession in Israel was deposited on the northern margin of Gondwana, facing the tropical western Tethys (Fig. 1). The studied interval includes the Ra′af and Gevanim formations (Fig. 2B and fig. S4).

U-Pb geochronology

Zircons were separated from a ~5-cm-thick ash bed in the middle part of the Ermaying Formation of the LY Section (CSS-4) and an ~2-cm-thick ash bed in the upper part of the XF Section (XF10-5) (Fig. 2). After pulverization using a shatter box, heavy minerals were separated using standard magnetic and high-density liquid separation techniques; several thousand zircon grains were obtained from the >2000g ash sample.

Eight (CSS-4) and Seven (XF10-5) prismatic and multifaceted zircon grains (some with axial glass inclusions) were selected under the binocular microscope and were analyzed by the U-Pb CA-ID-TIMS method. Zircons were analyzed at the University of Geneva, Switzerland, following the general analytical procedures described by (*62*). The selected zircons were pretreated by a chemical abrasion technique modified after (*63*), which involved thermal annealing at 950°C for 48 hours and partial dissolution in 28 M HF inside hydrothermal vessels at 210°C for 12 hours, to mitigate the effects of radiation-induced Pb loss. Thoroughly fluxed and rinsed grain were then spiked with the EARTHTIME ET2535 mixed ^{202}Pb-^{205}Pb-^{233}U-^{235}U tracer (*64*, *65*), before complete dissolution in HF for 48 hours followed by an anion-exchange column chemistry for purification of Pb and U. Measurements of the Pb and U isotopes were carried out on a TRITON mass spectrometer equipped with a MasCom discrete dynode electron multiplier in Geneva. Pb and UO_2 were measured in static mode using Faraday cups attached to 10^{13}-Ω resistors or when the beam signal was insufficient, the electron multiplier was used in dynamic peak jumping mode (data S1). The deadtime was determined to be constant at 22.5 ns for up to 1.3 Mcps and at a Faraday/SEM yield between 93 and 94%.

Isotopic data reduction, date calculation, and error propagation used the applications Tripoli and ET_Redux and their algorithms (*66*, *67*). Complete U-Pb isotopic data are given in data S1. All analyses were corrected for initial ^{230}Th disequilibrium using a value of 3.5 as the best estimate for the Th/U ratio of the parent magma. The ash bed age is calculated on the basis of the weighted mean ^{206}Pb/^{238}U date of zircons from the concordant analyses from each sample. For sample CSS4, analysis z1 was excluded because it plots outside the main data cluster and may reflect minor Pb loss (fig. S11A). For XF10-5, the youngest concordant age was selected for interpretation, whereas the older ages were excluded due to their likely association with heterogeneous zircon domains or inherited components (fig. S11B). The age uncertainty is reported and in the format $\pm x/y/z$ Ma, where x is the analytical (internal) uncertainty only, y includes the additional tracer calibration error, and z includes the latter as well as the ^{238}U decay constant error of (*68*). To compare the calculated age with those from other ID-TIMS U-Pb laboratories not using the EARTHTIME tracer (or from other U-Pb techniques), the $\pm y$ for either set of data must be taken into account. Ages from each of the studied samples were only calculated using concordant analysis (fig. S11).

Geochemical sample preparation

A total of 196 samples were collected for geochemical analysis, 43 mudstone samples from the LY section, 41 mudstone samples from the XF section, 26 carbonate samples from the YW section, 52 carbonate samples from the DT section, and 34 carbonate samples from the RM borehole. For geochemical analysis, we crushed the samples and sieved them to <200 μm. Samples from DT were analyzed for carbonate carbon isotopes ($\delta^{13}C_{carb}$). Samples from LY, XF, and DT were analyzed for TOC and TS. Samples from LY, XF and DT were analyzed for organic carbon isotopes ($\delta^{13}C_{org}$). Samples from LY, XF, DT, and RM were analyzed for mercury (Hg) concentrations. All these analyses were carried out at the State Key Laboratory of Geomicrobiology and Environmental Changes of China University of Geosciences, Wuhan. Considering both the sample distribution and the Hg concentration, a total of 31 samples were selected from the four sections (LY, YW, DT, and RM) for Hg isotope analysis at State Key Laboratory of Ore Deposit Geochemistry, Institute of Geochemistry, Chinese Academy of Sciences, Guiyang. All the geochemical data are given in data S2.

C isotopes, TOC, and TS

For the $\delta^{13}C_{carb}$ analyses, approximately 400 μg of powdered sample was extracted, placed in a 10-ml Na-glass vial, and sealed with a butyl rubber septum. The vial was then purged with helium and reacted with 100% phosphoric acid at 72°C. The $\delta^{13}C$ and $\delta^{18}O$ values of CO_2 were measured using a MAT253 mass spectrometer connected directly to the Finnigan Gasbench II interface (Thermo Fisher Scientific). The isotopic values are reported in per mille relative to the Vienna Pee Dee belemnite standard. The analytical precision was better than ±0.1 for $\delta^{13}C$ and ±0.1 for $\delta^{18}O$, as determined by replicate analyses of two laboratory standards, GBW04416 (with a $\delta^{13}C$ value of 1.61‰) and GBW04417 (−6.06‰).

For organic C-isotope analyses, powdered samples were decarbonated using 3 M HCl at 25°C for 24 hours. After, the sample was washed with deionized water until the solution was neutral and then dried at 45°C for 72 hours. Five to 20 mg of dried decarbonated sample was then weighed into tin capsules and combusted at 960°C. The generated CO_2 and N_2 were analyzed using a Flash HT 2000 Plus and continuous-flow Delta V Advantage IRMS (Thermo Fisher Scientific). International reference standards USGS40 ($\delta^{13}C_{VPDB} = -26.39‰$) and IVA-urea ($\delta^{13}C_{VPDB} = -37.32‰$) were analyzed for a two-point calibration. Analytical precision was better than 0.2‰ (1σ) for $\delta^{13}C$ based on replicate analyses of these standards.

Downloaded from https://www.science.org at University Studi Di Ferrara on June 19, 2026

An aliquot of decarbonated sample was used for the determination of TOC and TS. Approximately 100 mg of powdered sample was carefully weighed into a ceramic crucible, heated to 1750°C and analyzed using a 902 T C-S analyzer. The reproducibility of these analyses was better than 0.1%, based on replicate analyses of AR-4007 (with a TC of 7.62% and a TS of 3.27%) and AR-4017 (with a TC of 0.50 ± 0.03% and a TS of 0.48 ± 0.04%).

Mercury concentrations and isotopes

Hg concentrations in a total of 170 samples were analyzed using a Lumex RA-915+ Mercury Analyzer coupled to a PYRO-915+ pyrolyzer. RA-915M/PYRO-915 has a detection limit for sediments and rocks of 0.5 ppb (https://lumexinstruments.com). Powdered samples (20 to 100 mg) were weighed into a glass boat before being placed into the pyrolyzer and heated to 700°C. Throughout the measurement sequences (every five samples), CRM Stream Sediment (GSD-30; 148 ± 11 ppb Hg) standards were analyzed to evaluate the analytical error, which was determined to be ±5%.

Mercury isotope analysis methods refer to (*36*). The samples were preenriched with mercury by a double-stage tube furnace and the preconcentrated solutions are 5 ml of 40% anti aqua regia (HNO_3/HCl =2/1, v/v) (*69*). GSS-4 soil SRM ($n = 3$) was prepared in the same way as the samples. They were diluted to 1.0 ng/ml, with an acid concentration of 10 to 20% by using 18.2 MΩ cm water and then analyzed using the Neptune Plus Multicollector-Inductively Coupled Plasma Mass Spectrometer (Thermo Electron Corp, Bremen, Germany). NIST-8610 mercury standard solution, diluted to Hg (1.0 ng/ml) in 10% HCl, measured in the same way as the sample.

The mass-dependent fractionation (MDF) of the mercury isotope is expressed in δ^{202}Hg per mil (‰), referring to the Hg standard NIST-3133, the MDF before and after each sample is as follows

$$\delta^{202}\mathrm{Hg} = \left[\left(^{202}\mathrm{Hg}/^{198}\mathrm{Hg}_{\mathrm{sample}}\right)/\left(^{202}\mathrm{Hg}/^{198}\mathrm{Hg}_{\mathrm{standard}}\right) - 1\right] \times 1000 \quad (1)$$

The MIF for mercury isotopes is reported as Δ^{xxx}Hg, which describes the difference between the measured δ^{xxx}Hg and the theoretically predicted δ^{xxx}Hg value, in units per mil (‰), using the following formula

$$\Delta^{xxx}\mathrm{Hg} \approx \delta^{xxx}\mathrm{Hg} - \delta^{202}\mathrm{Hg} \times \beta \quad (2)$$

where β value is 0.2520 for ^{199}Hg, 0.5024 for ^{200}Hg, and 0.7520 for ^{201}Hg, respectively (*70*).

The overall average and uncertainty of GSS-4 (δ^{199}Hg: −0.83 ± 0.07‰; δ^{200}Hg: −0.86 ± 0.10‰; δ^{201}Hg: −1.65 ± 0.13‰; δ^{202}Hg: −1.71 ± 0.15‰; Δ^{199}Hg: −0.40 ± 0.04‰; Δ^{200}Hg: 0.00 ± 0.03‰; and Δ^{201}Hg: −0.36 ± 0.05‰, 2SD, $n = 3$) and NIST-8610 (δ^{199}Hg: −0.14 ± 0.05‰; δ^{200}Hg: −0.25 ± 0.03‰; δ^{201}Hg: −0.39 ± 0.04‰; δ^{202}Hg: −0.50 ± 0.02‰; Δ^{199}Hg: −0.02 ± 0.04‰; Δ^{200}Hg: 0.00 ± 0.03‰; and Δ^{201}Hg: −0.01 ± 0.04‰, 2SD, $n = 3$) agree well with previous results (*37*, *70*). Analytical uncertainty reported in this study corresponds to the larger value of replicate analyses of GSS-4 and NIST-8610.

Bayesian age-depth modeling and duration calculations

Bayesian age-depth model was constructed using the R package Bchron (*44*, *71*). CSS4 occurs before the onset of the PENCIE, whereas XF10-5 postdates the termination of the PENCIE; these dates were treated as control inputs in the age-depth model. Analytical ages, associated uncertainties, and stratigraphic positions were used to generate monotonic age-depth relationships via Markov chain Monte Carlo sampling. Posterior age distributions were predicted for horizons of interest, and mean ages with 95% credible intervals were calculated from the posterior estimates. Duration of PENCIE was calculated by subtracting posterior age distributions of bounding horizons on a sample-by-sample basis, thereby preserving covariance structure and uncertainty propagation. Posterior mean durations and 95% credible intervals were derived from these distributions.

Supplementary Materials

The PDF file includes:

Supplementary Text
Figs. S1 to S11
Legends for data S1 to S7
References

Other Supplementary Material for this manuscript includes the following:

Data S1 to S7

REFERENCES

1. Z.-Q. Chen, M. J. Benton, The timing and pattern of biotic recovery following the end-Permian mass extinction. *Nat. Geosci.* **5**, 375–383 (2012).
2. H. Song, P. B. Wignall, A. M. Dunhill, Decoupled taxonomic and ecological recoveries from the Permo-Triassic extinction. *Sci. Adv.* **4**, eaat5091 (2018).
3. A. Brayard, L. J. Krumenacker, J. P. Botting, J. F. Jenks, K. G. Bylund, E. Fara, E. Vennin, N. Olivier, N. Goudemand, T. Saucède, S. Charbonnier, C. Romano, L. Doguzhaeva, B. Thuy, M. Hautmann, D. A. Stephen, C. Thomazo, G. Escarguel, Unexpected Early Triassic marine ecosystem and the rise of the modern evolutionary fauna. *Sci. Adv.* **3**, e1602159 (2017).
4. X. Dai, J. H. F. L. Davies, Z. Yuan, A. Brayard, M. Ovtcharova, G. Xu, X. Liu, C. P. A. Smith, C. E. Schweitzer, M. Li, M. G. Perrot, S. Jiang, L. Miao, Y. Cao, J. Yan, R. Bai, F. Wang, W. Guo, H. Song, L. Tian, J. D. Corso, Y. Liu, D. Chu, H. Song, A Mesozoic fossil lagerstätte from 250.8 million years ago shows a modern-type marine ecosystem. *Science* **379**, 567–572 (2023).
5. D.-y. Jiang, M. Zhou, R. Motani, A. Tintori, N. C. Fraser, J.-d. Huang, O. Rieppel, C. Ji, W.-l. Fu, Z.-y. Sun, Emergence and ecological transition of the Mesozoic marine reptiles: Evidence from the Early Triassic Chaohu and the Middle Triassic Xingyi Faunas. *Palaeogeogr. Palaeoclimatol. Palaeoecol.* **628**, 111750 (2023).
6. A. J. Roberts, M. Rucinski, B. P. Kear, Ø. Hammer, V. S. Engelschiøn, T. H. Scharling, R. B. Larsen, J. H. Hurum, Earliest oceanic tetrapod ecosystem reveals rapid complexification of Triassic marine communities. *Science* **390**, 722–727 (2025).
7. Y. Sun, M. M. Joachimski, P. B. Wignall, C. Yan, Y. Chen, H. Jiang, L. Wang, X. Lai, Lethally hot temperatures during the Early Triassic greenhouse. *Science* **338**, 366–370 (2012).
8. S. E. Grasby, B. Beauchamp, A. Embry, H. Sanei, Recurrent early triassic ocean anoxia. *Geology* **41**, 175–178 (2013).
9. J. Chen, J. Tong, Z. Q. Chen, Brachiopod Assemblages from the early Middle Triassic of Qingyan, Guizhou, Southwest China. *J. Earth Sci.* **21**, 121–124 (2010).
10. M. J. Benton, Q. Zhang, S. Hu, Z.-Q. Chen, W. Wen, J. Liu, J. Huang, C. Zhou, T. Xie, J. Tong, B. Choo, Exceptional vertebrate biotas from the Triassic of China, and the expansion of marine ecosystems after the Permo-Triassic mass extinction. *Earth Sci. Rev.* **125**, 199–243 (2013).
11. S.-x. Hu, Q.-y. Zhang, Z.-Q. Chen, C.-y. Zhou, T. Lü, T. Xie, W. Wen, J.-y. Huang, M. J. Benton, The Luoping biota: Exceptional preservation, and new evidence on the Triassic recovery from end-Permian mass extinction. *Proc. Biol. Sci.* **278**, 2274–2282 (2011).
12. J. Liu, J. Ramezani, L. Li, Q.-H. Shang, G.-H. Xu, Y.-Y. Wang, J.-S. Yang, High-precision temporal calibration of Middle Triassic vertebrate biostratigraphy: U-Pb zircon constraints for the Sinokannemeyeria Fauna and Yonghesuchus. *Vertebr. PalAsiat.* **56**, 16–24 (2018).
13. W. Guo, L. Tian, D. Chu, W. Shu, M. J. Benton, J. Liu, J. Tong, Rapid riparian ecosystem recovery in low-latitudinal North China following the end-Permian mass extinction. *eLife* **14**, RP104205 (2025).
14. J. L. Payne, D. J. Lehrmann, J. Wei, M. J. Orchard, D. P. Schrag, A. H. Knoll, Large perturbations of the carbon cycle during recovery from the end-Permian extinction. *Science* **305**, 506–509 (2004).
15. Y. Isozaki, Permo-Triassic boundary superanoxia and stratified superocean: Records from lost deep sea. *Science* **276**, 235–238 (1997).
16. H. Song, P. B. Wignall, J. Tong, D. P. G. Bond, H. Song, X. Lai, K. Zhang, H. Wang, Y. Chen, Geochemical evidence from bio-apatite for multiple oceanic anoxic events during Permian–Triassic transition and the link with end-Permian extinction and recovery. *Earth Planet. Sci. Lett.* **353-354**, 12–21 (2012).

Downloaded from https://www.science.org at University Studi Di Ferrara on June 19, 2026

17. Y. Wu, A. Pohl, L. Tian, J. Dal Corso, Y. Cui, D. Chu, J. Tong, H. Song, H. Song, H. Song, Recurrent marine anoxia in the Paleo-Tethys linked to constriction of seaways during the Early Triassic. *Earth Planet. Sci. Lett.* **643**, 118882 (2024).
18. J. A. Trotter, I. S. Williams, A. Nicora, M. Mazza, M. Rigo, Long-term cycles of Triassic climate change: A new $\delta^{18}O$ record from conodont apatite. *Earth Planet. Sci. Lett.* **415**, 165–174 (2015).
19. S. E. Grasby, B. Beauchamp, J. Knies, Early Triassic productivity crises delayed recovery from world's worst mass extinction. *Geology* **44**, 779–782 (2016).
20. Y. Cao, D. Chu, J. Dal Corso, K. Wu, M. J. Benton, H. Song, H. Song, L. Tian, X. Dai, Y. Huang, X. Miao, S. Zhang, J. Tong, Pelsonian negative carbon isotope excursion (PENCIE): A Tethys-wide abnormal carbon cycle event in the Middle Triassic. *Palaeogeogr. Palaeoclimatol. Palaeoecol.* **654**, 112473 (2024).
21. E. Kustatscher, J. H. A. van Konijnenburg-van Cittert, G. Roghi, Macrofloras and palynomorphs as possible proxies for palaeoclimatic and palaeoecological studies: A case study from the Pelsonian (Middle Triassic) of Kühwiesenkopf/Monte Prà della Vacca (Olang Dolomites, N-Italy). *Palaeogeogr. Palaeoclimatol. Palaeoecol.* **290**, 71–80 (2010).
22. M. Stefani, S. Furin, P. Gianolla, The changing climate framework and depositional dynamics of Triassic carbonate platforms from the Dolomites. *Palaeogeogr. Palaeoclimatol. Palaeoecol.* **290**, 43–57 (2010).
23. M. Li, C. Huang, L. Hinnov, W. Chen, J. Ogg, W. Tian, Astrochronology of the Anisian stage (Middle Triassic) at the Guandao reference section, South China. *Earth Planet. Sci. Lett.* **482**, 591–606 (2018).
24. M. Ovtcharova, H. Bucher, U. Schaltegger, T. Galfetti, A. Brayard, J. Guex, New Early to Middle Triassic U–Pb ages from South China: Calibration with ammonoid biochronozones and implications for the timing of the Triassic biotic recovery. *Earth Planet. Sci. Lett.* **243**, 463–475 (2006).
25. E. Kustatscher, S. Manfrin, P. Mietto, R. Posenato, G. Roghi, New biostratigraphic data on Anisian (Middle Triassic) palynomorphs from the Dolomites, Italy. *Rev. Palaeobot. Palynol.* **140**, 79–90 (2006).
26. P. Mietto, S. Manfrin, A high resolution Middle Triassic ammonoid standard scale in the Tethys Realm; a preliminary report. *Bull. Soc. Géol. Fr.* **166**, 539–563 (1995).
27. J. G. Ogg, Z. Q. Chen, M. J. Orchard, H. S. Jiang, "The triassic period" in *Geologic time scale 2020* (Elsevier, 2020), pp. 903–953.
28. A. Parnes, I. Zak, Middle Triassic cephalopods from the Negev (Israel) and Sinai (Egypt). With an introduction on the Triassic period in Israel. *Bull. Geol. Surv. Isr.* **79**, 59 (1986).
29. C. Benjamini, Foraminifera from the Ra'af Formation (Anisian), Har'areif, western Negev, Israel. *Bull. Cent. Rech. Explor. Prod. Elf-Aquitaine Mém.* , 35–40 (1984).
30. F. Hirsch, Note on *Neospathodus* cf. *N. kockeli* (Tatge) (Conodonta) from Ramon 1 well, central Negev, Israel. *Israel J. Earth Sci.* **26**, 94–96 (1977).
31. A. L. Sun, Late Permian and Triassic terrestrial tetrapods of north China. *Vertebr. PalAsiat.* **18**, 100–110 (1980).
32. A. Schneider-Mor, T. Zilberman, D. Korngreen, Global and regional variations in tropical marine environments of Gondwana as revealed by a multi-stable isotope study, Middle Triassic (Anisian), Israel, Levant Basin. *Palaeogeogr. Palaeoclimatol. Palaeoecol.* **507**, 115–128 (2018).
33. S. E. Grasby, T. R. Them Ii, Z. Chen, R. Yin, O. H. Ardakani, Mercury as a proxy for volcanic emissions in the geologic record. *Earth Sci. Rev.* **196**, 102880 (2019).
34. M. Edmonds, E. Mason, O. Hogg, Volcanic outgassing of volatile trace metals. *Annu. Rev. Earth Planet. Sci.* **50**, 79–98 (2022).
35. J. D. Blum, L. S. Sherman, M. W. Johnson, Mercury isotopes in earth and environmental sciences. *Annu. Rev. Earth Planet. Sci.* **42**, 249–269 (2014).
36. R. Yin, X. Feng, J. P. Hurley, D. P. Krabbenhoft, R. F. Lepak, R. Hu, Q. Zhang, Z. Li, X. Bi, Mercury isotopes as proxies to identify sources and environmental impacts of mercury in sphalerites. *Sci. Rep.* **6**, 18686 (2016).
37. C. Deng, G. Sun, Y. Rong, R. Sun, D. Sun, B. Lehmann, R. Yin, Recycling of mercury from the atmosphere-ocean system into volcanic-arc–associated epithermal gold systems. *Geology* **49**, 309–313 (2021).
38. R. Yin, X. Wang, R. Sun, L. Gao, C. Deng, Z. Tian, A. Luo, B. Lehmann, Linking the mercury biogeochemical cycle to the deep mercury cycle: A mercury isotope perspective. *Chem. Geol.* **654**, 122063 (2024).
39. H. Song, P. B. Wignall, J. Tong, H. Song, J. Chen, D. Chu, L. Tian, M. Luo, K. Zong, Y. Chen, X. Lai, K. Zhang, H. Wang, Integrated Sr isotope variations and global environmental changes through the Late Permian to early Late Triassic. *Earth Planet. Sci. Lett.* **424**, 140–147 (2015).
40. W. Cao, C.-T. A. Lee, J. S. Lackey, Episodic nature of continental arc activity since 750 Ma: A global compilation. *Earth Planet. Sci. Lett.* **461**, 85–95 (2017).
41. H. Song, C. R. Scotese, The end-Paleozoic great warming. *Sci. Bull.* **68**, 2523–2526 (2023).
42. Y. Wang, X. Qian, P. A. Cawood, H. Liu, Q. Feng, G. Zhao, Y. Zhang, H. He, P. Zhang, Closure of the East Paleotethyan Ocean and amalgamation of the Eastern Cimmerian and Southeast Asia continental fragments. *Earth Sci. Rev.* **186**, 195–230 (2018).
43. S. Li, T. Wang, S. A. Wilde, Y. Tong, Evolution, source and tectonic significance of Early Mesozoic granitoid magmatism in the Central Asian Orogenic Belt (central segment). *Earth Sci. Rev.* **126**, 206–234 (2013).
44. A. C. Parnell, J. Haslett, J. R. M. Allen, C. E. Buck, B. Huntley, A flexible approach to assessing synchroneity of past events using Bayesian reconstructions of sedimentation history. *Quat. Sci. Rev.* **27**, 1872–1885 (2008).
45. C. Monnet, P. Brack, H. Bucher, H. Rieber, Ammonoids of the middle/late Anisian boundary (Middle Triassic) and the transgression of the Prezzo Limestone in eastern Lombardy-Giudicarie (Italy). *Swiss J. Geosci.* **101**, 61–84 (2008).
46. Z. Ma, S. Hu, H. Wu, X. Liu, C. Zhou, W. Wen, Q. Zhang, J. Huang, X. Min, High productivity promoted exceptional fossil preservation of the early Middle Triassic Luoping biota of Yunnan Province, China. *Palaeogeogr. Palaeoclimatol. Palaeoecol.* **607**, 111286 (2022).
47. D. P. G. Bond, S. E. Grasby, On the causes of mass extinctions. *Palaeogeogr. Palaeoclimatol. Palaeoecol.* **478**, 3–29 (2017).
48. S. E. Grasby, D. P. G. Bond, How large igneous provinces have killed most life on Earth—Numerous times. *Elements* **19**, 276–281 (2023).
49. J. Kasbohm, B. Schoene, S. Burgess, Radiometric constraints on the timing, tempo, and effects of large igneous province emplacement. *Large Igneous Provinces: A Driver of Global Environmental and Biotic Changes* (2021), pp. 27–82.
50. S. D. Burgess, S. Bowring, S.-z. Shen, High-precision timeline for Earth's most severe extinction. *Proc. Natl. Acad. Sci. U.S.A.* **111**, 3316–3321 (2014).
51. B. Schoene, J. Guex, A. Bartolini, U. Schaltegger, T. J. Blackburn, Correlating the end-Triassic mass extinction and flood basalt volcanism at the 100 ka level. *Geology* **38**, 387–390 (2010).
52. T. J. Blackburn, P. E. Olsen, S. A. Bowring, N. M. McLean, D. V. Kent, J. Puffer, G. McHone, E. T. Rasbury, M. Et-Touhami, Zircon U-Pb geochronology links the end-Triassic extinction with the Central Atlantic Magmatic Province. *Science* **340**, 941–945 (2013).
53. J.-X. Fan, S.-Z. Shen, D. H. Erwin, P. M. Sadler, N. M. Leod, Q.-M. Cheng, X.-D. Hou, J. Yang, X.-D. Wang, Y. Wang, H. Zhang, X. Chen, G.-X. Li, Y.-C. Zhang, Y.-K. Shi, D.-X. Yuan, Q. Chen, L.-N. Zhang, C. Li, Y.-Y. Zhao, A high-resolution summary of Cambrian to Early Triassic marine invertebrate biodiversity. *Science* **367**, 272–277 (2020).
54. M. Ruhl, N. R. Bonis, G.-J. Reichart, J. S. S. Damsté, W. M. Kürschner, Atmospheric carbon injection linked to end-Triassic mass extinction. *Science* **333**, 430–434 (2011).
55. Y. Chen, L. Krystyn, M. J. Orchard, X. L. Lai, S. Richoz, A review of the evolution, biostratigraphy, provincialism and diversity of Middle and early Late Triassic conodonts. *Pap. Palaeontol.* **2**, 235–263 (2016).
56. E. Friesenbichler, M. Hautmann, H. Bucher, The main stage of recovery after the end-Permian mass extinction: Taxonomic rediversification and ecologic reorganization of marine level-bottom communities during the Middle Triassic. *PeerJ* **9**, e11654 (2021).
57. A. Vörös, Ammonoid diversification in the Middle Triassic: Examples from the Tethys (Eastern Lombardy, Balaton Highland) and the Pacific (Nevada). *Cent. Eur. Geol.* **57**, 319–343 (2014).
58. F. Stiller, H. Bucher, Anisian ammonoids from Qingyan, southwestern China: Biostratigraphical implications for the age of the Qingyan Formation. *Swiss J. Geosci.* **101**, 547–562 (2008).
59. R. D. C. Bicknell, J. Žalohar, P. Miklavc, B. Celarc, M. Križnar, T. Hitij, Revisiting horseshoe crab fossils from the Middle Triassic (Anisian) Strelovec Formation Konservat-Lagerstätte of Slovenia. *Palaeontol. Electron.* **24**, a36 (2021).
60. S. E. Grasby, J. L. Crowley, M. T. Mohr, J. B. Percival, O. H. Ardakani, J. Galloway, M. Bringué, I. R. Smith, W. Yuan, Oceanic anoxic event 3 in Arctic Canada—Arc volcanism and ocean fertilization drove anoxia. *Geol. Soc. Am. Bull.* **137**, 411–426 (2025).
61. Z. Zhu, Y. Liu, H. Kuang, A. J. Newell, N. Peng, M. Cui, M. J. Benton, Improving paleoenvironment in North China aided Triassic biotic recovery on land following the end-Permian mass extinction. *Global Planet. Change* **216**, 103914 (2022).
62. X. Dai, M. Ovtcharova, J. H. F. L. Davies, H. Song, X. Liu, Z. Yuan, Y. Cao, R. Bai, D. Chu, J. Dal Corso, A. Brayard, S. Jiang, L. Miao, Y. Du, H. Song, Geochronology of the Early Triassic based on coupled Bayesian zircon eruption age and Bayesian age–depth models. *Proc. Natl. Acad. Sci. U.S.A.* **122**, e2509247122 (2025).
63. J. M. Mattinson, Zircon U–Pb chemical abrasion ("CA-TIMS") method: Combined annealing and multi-step partial dissolution analysis for improved precision and accuracy of zircon ages. *Chem. Geol.* **220**, 47–66 (2005).
64. D. J. Condon, B. Schoene, N. M. McLean, S. A. Bowring, R. R. Parrish, Metrology and traceability of U–Pb isotope dilution geochronology (EARTHTIME Tracer Calibration Part I). *Geochim. Cosmochim. Acta* **164**, 464–480 (2015).
65. N. M. McLean, D. J. Condon, B. Schoene, S. A. Bowring, Evaluating uncertainties in the calibration of isotopic reference materials and multi-element isotopic tracers (EARTHTIME Tracer Calibration Part II). *Geochim. Cosmochim. Acta* **164**, 481–501 (2015).
66. J. F. Bowring, N. M. McLean, S. A. Bowring, Engineering cyber infrastructure for U-Pb geochronology: Tripoli and U-Pb_Redux. *Geochem. Geophys. Geosyst.* **12**, Q0AA19 (2011).
67. N. M. McLean, J. F. Bowring, S. A. Bowring, An algorithm for U-Pb isotope dilution data reduction and uncertainty propagation. *Geochem. Geophys. Geosyst.* **12**, Q0AA18 (2011).
68. A. H. Jaffey, K. F. Flynn, L. E. Glendenin, W. C. Bentley, A. M. Essling, Precision measurement of half-lives and specific activities of ^{235}U and ^{238}U. *Phys. Rev. C* **4**, 1889–1906 (1971).
69. L. Gao, D. Sun, X. Wang, D. Chen, Z. Tian, A. Luo, R. Yin, A catalyst tube-equipped dual-stage tube furnace system for accurate Hg isotopic determination of ore samples

Downloaded from https://www.science.org at University Studi Di Ferrara on June 19, 2026

using neptune plus multicollector inductively coupled plasma mass spectrometry. *Anal. Chem.* **96**, 17560–17566 (2024).
70. J. D. Blum, B. A. Bergquist, Reporting of variations in the natural isotopic composition of mercury. *Anal. Bioanal. Chem.* **388**, 353–359 (2007).
71. B. Schoene, M. P. Eddy, K. M. Samperton, C. B. Keller, G. Keller, T. Adatte, S. F. R. Khadri, U-Pb constraints on pulsed eruption of the Deccan Traps across the end-Cretaceous mass extinction. *Science* **363**, 862–866 (2019).
72. C. R. Scotese, An atlas of Phanerozoic paleogeographic maps: The seas come in and the seas go out. *Annu. Rev. Earth Planet. Sci.* **49**, 679–728 (2021).
73. W. Shu, J. Tong, J. Yu, J. Hilton, M. J. Benton, X. Shi, J. B. Diez, P. B. Wignall, D. Chu, L. Tian, Z. Yi, Y. Mao, Permian–Middle Triassic floral succession in North China and implications for the great transition of continental ecosystems. *GSA Bull.* **135**, 1747–1767 (2023).
74. J. Chen, G. Sun, B. Lu, R.-y. Ma, Z. Xiao, Y.-f. Cai, H. Zhang, S.-z. Shen, F. Zhang, Z. Feng, Inconsistent mercury records from terrestrial upland to coastal lowland across the Permian-Triassic transition. *Earth Planet. Sci. Lett.* **614**, 118195 (2023).
75. T. Zambardi, J. E. Sonke, J. P. Toutain, F. Sortino, H. Shinohara, Mercury emissions and stable isotopic compositions at Vulcano Island (Italy). *Earth Planet. Sci. Lett.* **277**, 236–243 (2009).
76. R. Sun, D. G. Streets, H. M. Horowitz, H. M. Amos, G. Liu, V. Perrot, J.-P. Toutain, H. Hintelmann, E. M. Sunderland, J. E. Sonke, Historical (1850–2010) mercury stable isotope inventory from anthropogenic sources to the atmosphere. *Elementa* **4**, 000091 (2016).
77. M. Si, D. S. McLagan, A. Mazot, N. Szponar, B. Bergquist, Y. D. Lei, C. P. J. Mitchell, F. Wania, Measurement of atmospheric mercury over volcanic and fumarolic regions on the North Island of New Zealand using passive air samplers. *ACS Earth Space Chem.* **4**, 2435–2443 (2020).
78. H. Zhang, F. Zhang, J.-B. Chen, D. H. Erwin, D. D. Syverson, P. Ni, M. Rampino, Z. Chi, Y.-F. Cai, L. Xiang, W.-Q. Li, S.-A. Liu, R.-C. Wang, X.-D. Wang, Z. Feng, H.-M. Li, T. Zhang, H.-M. Cai, W. Zheng, Y. Cui, X.-K. Zhu, Z.-Q. Hou, F.-Y. Wu, Y.-G. Xu, N. Planavsky, S.-Z. Shen, Felsic volcanism as a factor driving the end-Permian mass extinction. *Sci. Adv.* **7**, eabh1390 (2021).
79. M. Jiskra, L.-E. Heimbürger-Boavida, M.-M. Desgranges, M. V. Petrova, A. Dufour, B. Ferreira-Araujo, J. Masbou, J. Chmeleff, M. Thyssen, D. Point, Mercury stable isotopes constrain atmospheric sources to the ocean. *Nature* **597**, 678–682 (2021).

Acknowledgments: We thank X. Miao, E. Jia, X. Liu, S. Zhang, and Y. Su for help in the field work. We also thank H. Song, Y. Huang, L. Tian, and K. Wu for helpful and constructive discussions. Y.C. acknowledges support from the China Scholarship Council (CSC). X.D. is grateful to the Alexander von Humboldt Foundation for a research fellowship. **Funding:** This work was supported by the National Key Research and Development Project of China grant 2023YFF0804100 (D.C.) and National Natural Science Foundation of China grants 42472021, 42325202, 92255303, and 42402003 (D.C., H.S., and X.D.). **Author contributions:** Conceptualization: D.C., Y.C., H.S., J.T., S.E.G., M.J.B., and G.R. Methodology: D.C., Y.C., J.D.C., R.Y., M.O., and S.E.G. Investigation: D.C., Y.C., M.O., J.D.C., P.G., and G.R. Validation: D.C., Y.C., X.D., R.Y., S.E.G., and M.O. Resources: D.C., Y.C., J.D.C., R.Y., M.O., D.K., and A.S.-M. Visualization: D.C. and Y.C. Data curation: D.C., Y.C., R.Y., and M.O. Project administration: D.C. and J.T. Formal analysis: D.C., Y.C., R.Y., and S.E.G. Software: X.D. Supervision: D.C., J.T., H.S., and S.E.G. Funding acquisition: D.C. and H.S. Writing–original draft: Y.C., D.C. Writing–review and editing: D.C., Y.C., H.S., J.D.C., X.D., G.A., R.Y., J.T., S.E.G., M.J.B., P.G., D.K., A.S.-M., M.C., and G.R. **Competing interests:** The authors declare that they have no competing interests. **Data, code, and materials availability:** All data needed to evaluate and reproduce the results in the paper are present in the paper and/or the Supplementary Materials. This study did not generate new materials. The samples used in this study are stored at State Key Laboratory of Geomicrobiology and Environmental Changes, School of Earth and Planetary Sciences, China University of Geosciences and are available from the corresponding author upon reasonable request.

Submitted 26 November 2025
Accepted 7 May 2026
Published 17 June 2026
10.1126/sciadv.aee2291

Downloaded from https://www.science.org at University Studi Di Ferrara on June 19, 2026

ScienceAdvances

A #0.5 Myr perturbation of carbon and mercury cycles during the Middle Triassic biotic radiation

Yiran Cao, Daoliang Chu, Runsheng Yin, Haijun Song, Jacopo Dal Corso, Maria Ovtcharova, Piero Gianolla, Stephen E. Grasby, Michael J. Benton, Xu Dai, Greta Alverà, Guido Roghi, Marcello Caggiati, Aya Schneider-Mor, Dorit Korngreen, and Jinnan Tong

Sci. Adv. **12** (25), eaee2291. DOI: 10.1126/sciadv.aee2291

View the article online
https://www.science.org/doi/10.1126/sciadv.aee2291
Permissions
https://www.science.org/help/reprints-and-permissions

Downloaded from https://www.science.org at University Studi Di Ferrara on June 19, 2026

Use of this article is subject to the Terms of service

Science Advances (ISSN 2375-2548) is published by the American Association for the Advancement of Science. 1200 New York Avenue NW, Washington, DC 20005. The title *Science Advances* is a registered trademark of AAAS.

Copyright © 2026 the authors; exclusive licensee American Association for the Advancement of Science subject to Canadian Crown copyright, © His Majesty the King in Right of Canada, as represented by the Minister of the Environment, 2026. Distributed under a Creative Commons Attribution NonCommercial License 4.0 (CC BY-NC).